Kondo et al. Progress in Earth and Planetary Science (2016) 3:25
DOI 10.1186/s40645-016-0099-0

Progress in Earth and Planetary Science

RESEARCH ARTICLE Open Access

Major element composition of an Early Enriched Reservoir: constraints from $^{142}Nd/^{144}Nd$ isotope systematics in the early Earth and high-pressure melting experiments of a primitive peridotite

Nozomi Kondo[1*], Takashi Yoshino[2], Kyoko N. Matsukage[1] and Tetsu Kogiso[1]

Abstract

The Accessible Silicate Earth (ASE) has a higher $^{142}Nd/^{144}Nd$ ratio than most chondrites. Thus, if the Earth is assumed to have formed from these chondrites, a complement low-$^{142}Nd/^{144}Nd$ reservoir is needed. Such a low-$^{142}Nd/^{144}Nd$ reservoir is believed to have been derived from a melt in the early Earth and is called the Early Enriched Reservoir (EER). Although the major element composition of the EER is crucial for estimating its chemical and physical properties (e.g., density) and is also essential for understanding the origin and fate of the EER, which are both major factors that determine the present composition of the Earth, it has not yet been robustly established. In order to determine the major element composition of the EER, we estimated the age and pressure–temperature conditions to form the EER that would best explain its Nd isotopic characteristics, based on Sm–Nd partitioning and its dependence on pressure, temperature, and melting phase relations. Our estimate indicates that the EER formed within 33.5 Myr of Solar System formation and at near-solidus temperatures and shallow upper-mantle pressures. We then performed high-pressure melting experiments on primitive peridotite to determine the major element composition of the EER at estimated temperature at 7 GPa and calculated the density of the EER. The result of our experiments indicates that the near-solidus melt is iron-rich komatiite. The estimated density of the near-solidus melt is lower than that of the primitive peridotite, suggesting that the EER melt would have ascended in the mantle to form an early crust. Given that high mantle potential temperatures are assumed to have existed in the Hadean, it follows that the EER melt was generated at high pressure and, therefore, its composition would have been picritic to komatiitic. As the formation age of the EER estimated in our study precedes the last giant, lunar-forming impact, the picritic to komatiitic crust (EER) would most likely have been ejected from the Earth by the last giant impact or preceding impacts. Thus, the EER has been lost, leaving the Earth more depleted than its original composition.

Keywords: ^{142}Nd anomaly, Early Enriched Reservoir, Hadean, Major element composition, Near-solidus melt, High-pressure melting experiment

* Correspondence: kondo.nozomi.75x@st.kyoto-u.ac.jp
[1]Graduate School of Human and Environmental Studies, Kyoto University, Yoshida-nihonmatsu-tyo, Sakyo-ku, Kyoto 606-8501, Japan
Full list of author information is available at the end of the article

Introduction

Recent ^{142}Nd analyses of terrestrial rocks and chondrites have revealed that terrestrial samples exhibit a nearly uniform $^{142}Nd/^{144}Nd$ ratio that is higher than most chondrites (Boyet and Carlson 2005; Jackson and Carlson 2012). Given that ^{142}Nd is generated through radioactive decay of ^{146}Sm, the high $^{142}Nd/^{144}Nd$ ratio of the terrestrial samples is attributed to either a high $^{146}Sm/^{144}Nd$ or initial $^{142}Nd/^{144}Nd$ ratio. A high $^{146}Sm/^{144}Nd$ ratio would require early silicate differentiation due to the short half-life of ^{146}Sm (68 Myr; Kinoshita et al. 2012), given the lithophile behavior of Sm and Nd, with Sm being less incompatible than Nd. As such, investigations of ^{142}Nd anomalies may be key to understanding planetary formation and mantle evolution in the early Earth.

Three major hypotheses have been proposed to explain the higher $^{142}Nd/^{144}Nd$ ratios of terrestrial rocks compared with most chondrites. The first hypothesis is that a low-Sm/Nd reservoir was formed in the early Earth, which was then either hidden and isolated from mantle convection or lost from the Earth. If we assume that the Earth formed with initial $^{142}Nd/^{144}Nd$ and Sm/Nd ratios similar to most chondrites, then a low-$^{142}Nd/^{144}Nd$ reservoir would be necessary to compensate for the high $^{142}Nd/^{144}Nd$ ratio of terrestrial samples. The low-$^{142}Nd/^{144}Nd$ reservoir must have had a low $^{146}Sm/^{144}Nd$ ratio at its time of formation and is thought to have been formed as a silicate melt in the early Earth (Boyet and Carlson 2005). In this context, the low-$^{146}Sm/^{144}Nd$ reservoir is called the Early Enriched Reservoir (EER; Boyet and Carlson 2005), and it appears to be missing from the present-day Earth. In contrast, the residue produced during the EER formation is called the Early Depleted Reservoir (EDR; Boyet and Carlson 2005). Given that the EER is key to understanding silicate differentiation in the early Earth, the composition of the EER and the mechanisms, timing, and place of its formation have been extensively investigated. Boyet and Carlson (2005) and Korenaga (2009a) estimated the trace element composition of the EER based on mass-balance calculations of chondrites, EDR, and continental crust and concluded that the EER would have been generated at upper-mantle conditions. In particular, Boyet and Carlson (2005) argued that the EER would have had a similar composition to lunar KREEP rocks, which are enriched in potassium (K), rare earth elements (REE), and phosphorus (P) and are considered to have formed in the shallow mantle beneath the lunar anorthositic crust. However, the temperature and pressure conditions to form the EER have not been properly constrained. Labrosse et al. (2007) proposed that the existence of a basal magma ocean, which could be the "missing reservoir", can explain the difference in the $^{142}Nd/^{144}Nd$ ratios between chondrites and ASE. They estimated the trace element composition of the basal magma ocean using partition coefficients between Mg-perovskite and melt, which were experimentally determined at the uppermost lower-mantle pressures (Corgne et al. 2005). Lee et al. (2007) investigated the trace element systematics in natural Fe–O–S magmas and proposed that a similar Fe–O–S melt, which can account for the difference between the $^{142}Nd/^{144}Nd$ ratios of chondrites and the ASE, had formed during the final stages of magma ocean solidification. However, these previous studies mainly focused on the trace element composition of the EER, and the pressure and temperature conditions required to form the EER and its major element composition remain unconstrained.

The second hypothesis is that the Earth was formed from high-Sm/Nd materials, together with the Moon and Mars. Based on the $^{142}Nd/^{144}Nd$ and Sm/Nd ratios of lunar and Martian samples, Caro et al. (2008) argued that bulk Moon and Mars have high Sm/Nd ratios almost identical to the ASE and proposed that the Earth, Moon, and Mars were all formed from similarly high-Sm/Nd materials that had experienced partial melting and impact-erosion of crust during collisions with planetesimals. In this model, there is no need to develop models for the formation of the EER or the missing low-Sm/Nd reservoir through solidification of a terrestrial magma ocean (Caro 2011). However, the isotope ratios of lunar and Martian rocks observed on the surface of these bodies need to be corrected for the effect of exposure to cosmic rays, which is not straightforward. As such, it has even been argued that the lunar and Martian rocks have chondritic Sm/Nd ratios (Sprung et al. 2013). At present, the bulk compositions of the Moon and Mars remain imprecisely determined. Moreover, the fractionation between Sm and Nd associated with silicate differentiation during planetesimal collisions is also an unknown factor (Weiss and Elkins-Tanton 2013).

The third hypothesis is that the Earth accreted from material with different nucleosynthetic Sm or Nd than that of chondrites. Previous studies have revealed that ordinary chondrites (OC) and carbonaceous chondrites (CC) have average $^{142}Nd/^{144}Nd$ ratios that are 20 and 40 ppm lower than the ASE, respectively, and that enstatite chondrites (EC) have an average $^{142}Nd/^{144}Nd$ ratio that is ca. 10 ppm lower than the ASE, with some EC having $^{142}Nd/^{144}Nd$ ratios that overlap the terrestrial standard (Boyet and Gannoun 2013). These variations in $^{142}Nd/^{144}Nd$ ratios can be generated by p-, s-, and r-processes and have been interpreted to be the result of imperfect homogenization during the formation of the solar nebula (Qin and Carlson 2016). However, even after corrections for the effects of p-, s-, and r-processes, offsets can still be found among the $^{142}Nd/^{144}Nd$ ratios in chondrites and that of the terrestrial standard (Qin

and Carlson 2016). For this model involving the heterogeneous isotopic compositions of chondrites, the material that formed the Earth needs to be identified. In order to determine the Earth's accretionary material, previous studies have investigated differences in various stable isotope systems such as O and Si (Drake and Righter 2002; Fitoussi and Bourdon 2012). Assuming that changes in stable isotope ratios are negligible during core–mantle and mantle–crust differentiation, the stable isotope ratios of the ASE should represent those of the source material. Therefore, a chondrite that has stable isotope ratios identical to the ASE might have been the source of accretionary material for the Earth. Unfortunately, no such material has yet been identified.

Each of the above three hypotheses has both strengths and weaknesses, and it is currently unclear as to which is most plausible. In this study, we focus on the missing reservoir hypothesis, which we investigate by combining two novel approaches. The first is to constrain the melt fraction and pressure–temperature conditions required to form the EER from Sm–Nd systematics, experimentally determined phase relations of peridotite melting, and precise mineral–melt partition coefficient data. The second is to determine the major element composition of the EER by performing high-pressure melting experiments on primitive peridotites at the estimated pressure–temperature conditions. The major element composition of the EER allows us to estimate the physical and chemical characteristics of the EER, such as density, viscosity, and contents of heat-producing elements (e.g., K). One of the aims of this study is to determine the density of the EER, since this is essential for determining whether the EER would have been subducted and become hidden in the mantle or would have ascended to the surface and then lost from the Earth. Using these novel approaches, we construct a plausible model of the formation of the EER and explain the difference in $^{142}Nd/^{144}Nd$ ratios between the ASE and chondrites, investigate the silicate differentiation of the early Earth, and constrain the composition of the bulk silicate Earth (BSE).

Conditions necessary to form the EER

Here, we estimate the conditions required to form the EER assuming that the difference between the present-day $^{142}Nd/^{144}Nd$ ratios of chondrites and the ASE reflects variable Sm/Nd ratios generated during the formation of the EER in the early Earth. If the EER originated from a melt, then the difference in Sm/Nd ratios between chondrites and the ASE should reflect the melting conditions under which the EER formed, such as the degree of melting, mineral assemblage and proportion of the residual solid, and partition coefficients. Given that these parameters are dependent on pressure and temperature, we can then estimate the pressure and temperature conditions under which the EER formed.

We assumed a simple box model involving mass-balance calculations where (1) the whole region corresponding to fraction X of the mantle with a chondritic, primitive mantle composition (Chondritic Uniform Reservoir (CHUR)) experienced a single partial melting event with melt fraction F and differentiated into a melt (EER) and residual solid (EDR) in the early Earth (Fig. 1); (2) EER remained isolated until the present; (3) and ASE formed as a mixture of the EDR and an intact region in the mantle. Based on these assumptions, the difference between the Sm/Nd ratios of the EDR and CHUR during formation of the EER can be traced back from the present-day $^{142}Nd/^{144}Nd$ ratios of ASE and CHUR (Fig. 1) using the following equation:

$$\left(\frac{^{142}Nd}{^{144}Nd}\right)_{t_p} = \left(\frac{^{142}Nd}{^{144}Nd}\right)_{tf} + \left(\frac{^{146}Sm}{^{144}Nd}\right)_{tf}\left(1-e^{-\lambda^{146}\left(t_p-t_f\right)}\right) \quad (1)$$

where t_f and t_p are the age of the EER formation and time since the formation of the Solar System, respectively. Then, the difference between the Sm/Nd ratios of EDR and CHUR can be expressed using the relationship among solid phase proportions, melt fraction, and mineral–melt partition coefficients as follows:

$$\frac{\left(\frac{^{146}Sm}{^{144}Nd}\right)_{t_f}^{EDR}}{\left(\frac{^{146}Sm}{^{144}Nd}\right)_{t_f}^{CHUR}} = \frac{\left(\frac{^{146}Sm^{EDR}}{^{146}Sm^{CHUR}}\right)_{t_f}}{\left(\frac{^{142}Nd^{EDR}}{^{142}Nd^{CHUR}}\right)_{t_f}} = \frac{\frac{D_{Sm}-\Pi_{Sm}F}{(1-F)(D_{Sm}+F-\Pi_{Sm}F)}}{\frac{D_{Nd}-\Pi_{Nd}F}{(1-F)(D_{Nd}+F-\Pi_{Nd}F)}} \quad (2)$$

The right-hand side of Eq. (2) represents partitioning of Sm and Nd between the source rock and the residual solid (Shaw 1970). D_i is the bulk partition coefficient of element i obtained by assuming that the proportion of minerals does not change during partial melting. In reality, the mineral proportions do change as partial melting progresses, and Π_i is the partition coefficient of element i obtained from the proportion of minerals entering the melt (Shaw 1970). F is the melt fraction. Given that the left-hand side of Eq. (2) is dependent on Eq. (1), we can obtain the melt fraction as a function of t_f. We used the $^{142}Nd/^{144}Nd$ ratios of the present-day terrestrial standard and the average value of ordinary chondrites (Boyet and Carlson 2005) in the calculations. The melt fraction was obtained as a function of t_f for two cases where the source region corresponds to the upper mantle ($X = 0.3$) and whole mantle ($X = 1$), respectively.

To determine Π_i and D_i, we must first obtain the pressure conditions for the EER formation, as melting phase relations and mineral–melt partition coefficients are dependent on pressure. In this study, we assumed that the EER formed at shallow, upper-mantle pressures because previously estimated trace element abundances of the EER resemble those of a melt generated in the upper

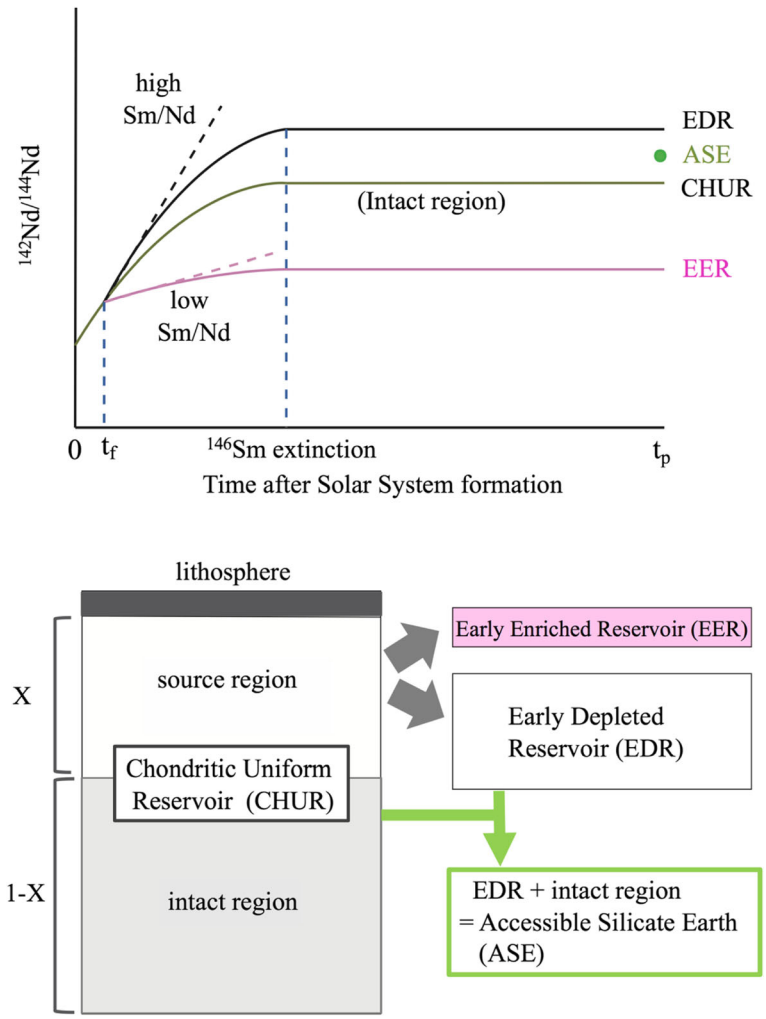

Fig. 1 Schematic illustrations of EER formation. (*Top*) The $^{142}Nd/^{144}Nd$ evolution considered in this study. A source region differentiates into the EER and EDR. The EER is hidden within or has been lost from the Earth. The EDR and intact region were mixed to form the ASE. (*Bottom*) A box model of the EER formation, where *X* is the fraction of the source region relative to the whole mantle. *ASE* Accessible Silicate Earth (part of the silicate Earth from which we can obtain materials for analysis), *EER* Early Enriched Reservoir (low-Sm/Nd reservoir which can compensate for the $^{142}Nd/^{144}Nd$ difference between ASE and chondrites), *EDR* Early Depleted Reservoir (residual solid produced by the EER formation), *CHUR* Chondritic Uniform Reservoir (putative primitive mantle having a chondritic composition)

mantle (Korenaga 2009a) and, in particular, the upper few hundred kilometers where clinopyroxene is stable (Boyet and Carlson 2005). We then performed our model calculations at three pressure conditions of 1, 3, and 7 GPa. In our model calculations, we need precise partition coefficients and quantitative melting phase relations; i.e., quantitative values for the proportions of solid phases that change as partial melting progresses. While precise partition coefficients have been determined experimentally up to 20 GPa (Nielsen et al. 1992; Salters and Longhi 1999; Frei et al. 2009; Suzuki et al. 2012), data for the quantitative melting phase relations are presently only available at 1, 3, and 7 GPa (Baker and Stolper 1994; Walter 1998), and thus, we have limited our model calculations to these pressures. It is not our intent to preclude the possibility that EER formation occurred at pressures >7 GPa, but this can only be explored when more precise experimental data on quantitative melting phase relations become available for pressures >7 GPa. The partition coefficients for our model calculations are listed in Table 1. The melting phase relations for each pressure were calculated from changes in mass proportions of phases between two temperatures following the method of Walter et al. (1995) (Appendix 1).

The calculated melt fraction is expressed as a function of the timing of the formation of the EER for each pressure condition (Fig. 2). A delay in the formation of the EER would necessitate a larger melt fraction. Therefore, it is essential to constrain the

Table 1 Partition coefficients for Sm and Nd and modal abundances of major mineral phases

	Whole rock mode	Partition coefficient Sm	Partition coefficient Nd	Partition coefficient ref.
7 GPa	Walter (1998)			
ol	54 %	0.001	0.000	Nielsen et al. (1992)
opx				
cpx	29 %	0.053	0.031	Suzuki et al. (2012)
gr	17 %	0.130	0.031	Suzuki et al. (2012)
3 GPa	Walter (1998)			
ol	53 %	0.001	0.000	Nielsen et al. (1992)
opx	18 %	0.017	0.008	Frei et al. (2009)
cpx	27 %	0.135	0.085	Suzuki et al. (2012)
gr	2 %	0.236	0.063	Suzuki et al. (2012)
1 GPa	Baker & Stolper (1994)			
ol	50 %	0.001	0.000	Nielsen et al. (1992)
opx	30 %	0.023	0.010	Frei et al. (2009)
cpx	17 %	0.494	0.258	Salters & Longhi (1999)

timing of the EER formation in order to constrain the melt fraction of the EER. We calculated the timing of the EER formation using the method of Boyet and Carlson (2005). We applied Eq. (1) to the ^{147}Sm–^{143}Nd and ^{146}Sm–^{142}Nd systematics and obtained an equation for t_f and $(Sm/Nd)_{tf}$. The following expression can be used to obtain t_f:

$$\frac{\left(\frac{^{146}Sm}{^{144}Nd}\right)_{t_f}^{ASE}}{\left(\frac{^{146}Sm}{^{144}Nd}\right)_{t_f}^{CHUR}} = \frac{\left(\frac{^{147}Sm}{^{144}Nd}\right)_{t_f}^{ASE}}{\left(\frac{^{147}Sm}{^{144}Nd}\right)_{t_f}^{CHUR}} \quad (3)$$

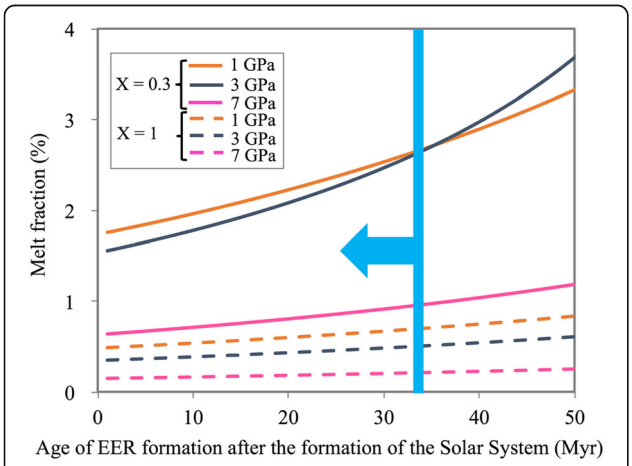

Fig. 2 Calculated melt fraction as a function of the formation age of the EER. *Bold* and *dashed lines* show melt fractions for the case of $X = 0.3$ and 1, respectively. The *blue bar* indicates the maximum formation age of the EER. *EER* Early Enriched Reservoir (low-Sm/Nd reservoir which can compensate for the ^{142}Nd/^{144}Nd difference between ASE and chondrites)

We used the average ^{143}Nd/^{144}Nd ratio of the source mantle of mid-ocean ridge basalt (MORB; $\frac{^{143}Nd}{^{144}Nd} = 0.513151$; $\varepsilon^{143}Nd = 10$) as the maximum value of ^{143}Nd/^{144}Nd in the ASE and obtained the maximum formation time of the EER. As a result, the formation of the EER is expected to be within 33.5 Myr of Solar System formation, which is broadly consistent with estimates in previous studies (30 Myr in Boyet and Carlson 2005; 20 Myr in Caro 2011).

We then obtained the maximum melt fraction from our method, for each pressure condition, and for the two different source fractions (Fig. 2). In the case where the source region is limited to the upper-mantle region ($X = 0.3$), the maximum melt fractions are 2.7 % at 1 GPa, 2.6 % at 3 GPa, and 1.0 % at 7 GPa. In the case where the source is the whole mantle ($X = 1$), the maximum melt fractions are 0.7 % at 1 GPa, 0.5 % at 3 GPa, and 0.2 % at 7 GPa, respectively. In these results, the maximum melt fractions become smaller at higher pressures. At a higher pressure, an increase in the proportion of garnet increases the D_{Sm}/D_{Nd} ratios of the whole rocks. Therefore, in order to achieve the $(^{142}Nd/^{144}Nd)^{EDR}/(^{142}Nd/^{144}Nd)^{CHUR}$ ratio, a smaller $(Sm/Nd)^{EDR}/(Sm/Nd)^{CHUR}$ is needed for higher pressures (larger D_{Sm}/D_{Nd}). In Eq. (2), $(Sm/Nd)^{EDR}/(Sm/Nd)^{CHUR}$ decreases with decreasing melt fraction. Therefore, the maximum melt fraction becomes smaller with increasing pressure, due to a larger proportion of garnet in the mantle peridotite. Based on the calculations presented in this section, we conclude that the EER should have been generated at very small degrees of partial melting, irrespective of whether the source was the upper or whole mantle. We discuss later the conditions that might enable such small degrees of Hadean melting.

Experimental determination of near-solidus melt compositions

We calculated the melt fractions to form the EER at 1, 3, and 7 GPa because the melting phase relations of a peridotite having primitive-mantle-like compositions have been determined precisely at these pressures by previous experimental studies (Baker and Stolper 1994 for 1 GPa; Walter 1998 for 3 and 7 GPa). Our results show that formation of the EER requires a small degree of melting near the solidus at these pressures. In this section, we determine the major element compositions of near-solidus melts formed at 1, 3, and 7 GPa based on high-pressure melting experiments of primitive peridotite. The near-solidus melt composition of a primitive peridotite at 1 GPa has been determined by Falloon et al. (2008) with the sandwich method (Takahashi and Kushiro 1983) using a fertile peridotite composition (MM3). The near-solidus melt composition at 3 GPa has been determined by Davis et al. (2011) following the Modified Iterative Sandwich Experiment method (MISE; Hirschmann and Dasgupta 2007). Herein, we determined the major element composition of a near-solidus melt of primitive peridotite at 7 GPa with the MISE method.

High-pressure experiment design

In order to determine the near-solidus melt composition at 7 GPa, we employed the MISE method proposed by Hirschmann and Dasgupta (2007). The steps involved in the MISE method are as follows:

(1) Equilibrating a putative near-solidus melt with peridotite at solidus temperature
(2) Determining a mineral–melt partition coefficient for each element based on the compositions of the resulting quenched melt and residual minerals
(3) Calculating a new putative near-solidus melt composition using a set of partition coefficients for each element in each mineral, the modal mineral assemblage of the peridotite, and the composition of the starting peridotite
(4) Synthesizing a new putative near-solidus melt

Steps (1)–(4) are performed repeatedly until a near-solidus melt is produced (for more details, see Hirschmann and Dasgupta 2007). The method for assessing whether a near-solidus melt composition has been achieved will be described later.

Experimental procedure

Starting materials

We used KLB-1 as the starting material for the peridotite component, as KLB-1 peridotite is considered to represent a fertile peridotite in the present-day mantle (Takahashi 1986), and its major element composition resembles that of the estimated primitive mantle (Ringwood 1966; McDonough and Sun 1995). The first putative near-solidus melt composition was calculated from an experimentally determined relationship between melt compositions and melt fractions of fertile peridotite at 7 GPa in Walter (1998). Powders of KLB-1 and putative near-solidus melt compositions were synthesized from reagent grade oxides and carbonates. The compositions of the synthesized starting powders are shown in Table 2. Powders of SiO_2, TiO_2, Al_2O_3, Cr_2O_3, Fe_2O_3, $CaCO_3$, Na_2CO_3, K_2CO_3, and $Ca_3(PO_4)_2$ were dried at 110 °C under atmospheric pressure for 24 h. MgO was dried at 1000 °C for at least 12 h, and MnO was kept in a vacuum at room temperature to prevent oxidation to MnO_2. These powders of oxides and carbonates were weighed with an electronic balance, and the powders, apart from Fe_2O_3, were mixed in an agate mortar with ethanol for 1 to 2 h. The mixture was placed in a Pt vessel and decarbonated in air by raising the temperature at a rate of 100 °C/h to 1100 °C and then held at that temperature for 24 h. After decarbonation, Fe_2O_3 was added and mixed in with an agate mortar under dry conditions. Pellets of the starting powders were then made and heated at the oxygen fugacity of iron–wüstite in a small Pt basket in a gas-mixing furnace at the Graduate School of Science, Kyoto University. Several pellets were stacked in a Pt basket, and the lowermost pellet in contact with the Pt was discarded to eliminate the effect of Fe-loss to the Pt. The pellets of the KLB-1 composition were heated at 1100 °C for 12 h, and pellets of the putative near-solidus melt composition were heated at 1000 °C for 12 h. The pellets were then first milled in a tungsten carbide mortar and subsequently ground in an agate mortar for 1 h. The starting powders were stored at 80 °C under vacuum to inhibit adsorption of atmospheric water. The H_2O contents in the starting materials were analyzed using a Karl Fischer Moisture Titrator MKC-610 at the Earthquake Research Institute, University of Tokyo (Table 2). From these analyses, it was confirmed that the starting materials contain negligible amounts of water.

High-pressure experiments

High-pressure experiments were performed at 7 GPa using 1000 and 5000 T Kawai-type multi-anvil apparatus at the Institute for Study of the Earth's Interior, Okayama University. Pressure was generated using eight tungsten carbide cubes with side lengths of 32 mm and truncated edge lengths of 8 mm and semi-sintered MgO (+5 wt% Cr_2O_3) octahedral pressure medium with edge lengths of 14 mm. The relationship between load and sample pressure was calibrated at 1600 °C using the following phase transformations: quartz–coesite at 3.7 GPa (Kanzaki 1990); coesite–stishovite at 10.26 GPa (Zhang

Table 2 Compositions of starting materials

wt%	KLB-1[a]	Primitive peridotite[b]	Putative solidus melt 1	Putative solidus melt 2	Putative solidus melt 3	Putative solidus melt 4	Putative solidus melt 5
SiO_2	44.48	44.61	43.8	45.3	43.8	44.4	44.3
TiO_2	0.16	0.17	2.5	1.8	1.5	1.6	1.9
Al_2O_3	3.59	3.60	4.9	5.1	5.4	5.3	4.3
Cr_2O_3	0.31	0.30	0.3	0.3	0.3	0.3	0.2
FeO	8.10	8.12	12.8	13.1	13.0	12.6	14.4
MnO	0.12	0.12	0.2	0.2	0.2	0.2	0.2
MgO	39.22	39.32	22.0	23.6	23.6	23.3	24.2
CaO	3.44	3.43	10.0	8.3	10.0	9.2	8.8
Na_2O	0.30	0.30	1.4	1.2	1.3	1.3	1.3
K_2O	0.02	0.02	1.5	1.0	0.6	1.5	0.2
P_2O_5	0.03	0.03	0.6	0.3	0.3	0.3	0.3
Total	99.8	100.00	100.0	100.0	100.0	100.0	100.0
Mg#	89.6	89.6	75.4	76.3	76.3	76.7	75.0
H_2O		0.07	0.08	0.07	0.07	0.06	0.08

[a]Takahashi (1986)
[b]This study

et al. 1996); Mg_2SiO_4 (α–β) at 15.2 GPa (Katsura et al. 2004). The starting material was packed in a Re capsule and then sealed in a Pt capsule. The sample capsule was placed in a MgO sleeve to insulate it from the straight $LaCrO_3$ heater. The junction of the WRe_3–WRe_{25} thermocouple and the sample capsule were positioned symmetrically relative to the center of the heater. The run durations at target temperature were 0.3–4.5 h. After quenching, the capsule was mounted in epoxy resin and polished with SiC and diamond powder. The polished sample was coated with carbon, and its chemical composition analyzed with an electron microprobe. We measured the temperature distribution in the capsule using two-pyroxene thermometry and confirmed that the temperature gradient was negligible (Appendix 2). The difference between temperatures from the thermocouple and two-pyroxene thermometry is within the range of the uncertainty of the two-pyroxene thermometer (~30 °C; Gasparik 1989).

Analytical procedures

Textural observations were made using a Hitachi S3500H scanning electron microscope, and quantitative analysis of major elements in minerals and melts was performed using a JEOL JXA-8100 electron microprobe equipped with five wavelength-dispersive spectrometers (WDS) at the Graduate School of Science, Kyoto University. Analytical conditions were based on the method of Kawakami and Hokada (2010). For the WDS quantitative analysis, an accelerating voltage of 15 kV and a ZAF matrix correction routine were used. The beam size was 3 μm for minerals and 10–15 μm for the melt in order to avoid heterogeneity effects. The beam current was 20 nA for the minerals and 10 nA for the melt. The mineral analyses used counting durations for peaks and backgrounds of 30 and 15 s for TiO_2, K_2O, and P_2O_5 and 10 and 5 s for other elements, respectively. The melt analyses used counting durations for peaks and backgrounds of 30 and 15 s for P_2O_5 and 10 and 5 s for other elements, respectively. Standard deviations were calculated from the analysis of >15 grains of each residual mineral and from >5 melt analyses. The phase proportions were obtained from mass-balance calculations using the composition of the coexisting phases, bulk composition, and least-squares method. Two conditions were utilized in the calculations, which involved including (or not) FeO, and the result with the smaller sum of squared residuals in the calculations was chosen. In the cases where FeO was included, Fe-loss was considered to be negligible.

Experimental results

Determination of solidus temperature and mineral compositions

Experiments to determine the solidus temperature and mineral compositions of KLB-1 at 7 GPa were performed at 1700, 1750, and 1800 °C. There was no melt in the quenched sample at 1700 °C, and the texture was homogeneous throughout the entire capsule. A large melt pool was present at 1800 °C. At 1750 °C, a small melt pool formed on the thermocouple side of the capsule (i.e., the hot side of the capsule). In the middle of the capsule, which was positioned symmetrically to the thermocouple junction with respect to the center of the

heater, a small amount of melt was observed between mineral boundaries. From these results, we concluded that the solidus temperature is just below 1750 °C. At this temperature, olivine, garnet, and clinopyroxene (cpx) were present, but orthopyroxene (opx) was not observed. This observation is consistent with the result of Walter (1998), which reported that opx is unstable near the solidus at 7 GPa at primitive mantle compositions. The chemical compositions of the solidus minerals were determined from the run at 1700 °C because even the presence of a small volume of melt at 1750 °C would likely affect the composition of the coexisting minerals. The compositions of the solidus minerals are summarized in Table 3. The Mg# ($100 \times Mg/(Mg + Fe)$) of the olivine, cpx, and garnet are 89.5, 89.6, and 86.0, respectively. The calculated mineral proportions are olivine:cpx:garnet = 63.3:22.8:13.9 (in wt%). No Fe-loss was evident in the run at 1700 °C.

Approach to the solidus melt composition

The MISE experiments were performed at 7 GPa and 1750 °C for both the primitive peridotite and putative near-solidus melt composition. In these experiments, we succeeded in obtaining melt and solidus mineral phases of olivine, cpx, and garnet. The experimental results are summarized in Table 4, and the analyzed compositions of the quenched melts and residual minerals are summarized in Table 5. There was no Fe-loss in the MISE iterations (Table 4). The Fe–Mg exchange partition coefficients between residual olivine and quenched melt were obtained and compared with those calculated from the ratio of non-bridging oxygens to tetrahedral cations (NBO/T) of the melts using the method of Mibe et al. (2006). The Fe–Mg exchange coefficients in the MISE iterations agree within uncertainties with an equilibrium exchange partition coefficient of 0.33.

Table 3 Compositions of minerals at the solidus

wt%	ol ($n = 15$)	s.d.[a]	cpx ($n = 15$)	s.d.	grt ($n = 15$)	s.d.
SiO_2	41.6	0.3	56.9	0.3	44.6	0.5
TiO_2	0.0	0.0	0.0	0.0	0.2	0.0
Al_2O_3	0.2	0.0	2.5	0.1	20.8	0.7
Cr_2O_3	0.1	0.1	0.3	0.1	1.8	0.8
FeO	10.2	0.4	5.2	0.2	6.6	0.3
MnO	0.1	0.0	0.1	0.0	0.2	0.0
MgO	48.9	0.4	25.2	0.9	22.6	0.4
CaO	0.3	0.1	9.4	1.0	4.8	0.4
Na_2O	0.1	0.0	0.9	0.0	0.1	0.0
K_2O	0.0	0.0	0.1	0.0	0.0	0.0
P_2O_5	0.0	0.0	0.0	0.0	0.1	0.0
Total	101.6	0.6	100.6	0.4	101.6	0.5
Mg#	89.5		89.6		86.0	

[a]Standard deviation (s.d.) is 1σ

In order to assess whether or not the composition of a quenched melt after an iteration step has sufficiently approached the composition of the true near-solidus melt, Dasgupta and Hirschmann (2007) and Davis et al. (2011) monitored the convergence of the residual mineral compositions to the solidus mineral compositions and the convergence of the mineral–melt partition coefficients and compositions of all phases to a steady state. In addition, Davis et al. (2011) monitored the difference between the analyzed and calculated melt compositions at each iteration step in order to identify equilibrium. However, using the MISE method, we consider that the conditions for generating the near-solidus melt composition can be obtained if there is (1) coincidence of the residual mineral compositions with the solidus mineral compositions and (2) convergence occurs between the analyzed and calculated melt compositions for the next step. Thus, satisfaction of both criteria 1 and 2 at step n is a sufficient condition to obtain the true near-solidus melt composition after the nth iteration. Figure 3 shows the analyzed melt compositions and calculated melt composition for the next step, and Fig. 4 shows the convergence of the chemical compositions of the residual minerals. The difference between the analyzed and calculated melt compositions for the next step diminished at the 5th iteration, and the chemical compositions of residual minerals reached those of the solidus minerals within error at the 5th iteration. From these results, it was concluded that the two criteria were satisfied at the 5th step, so that the calculated melt composition after the 5th iteration is taken to be the near-solidus melt composition.

Major element composition of the near-solidus melt

The major element composition of the near-solidus melt at 7 GPa (this study) is shown together with the near-solidus compositions experimentally obtained at 3 GPa (Davis et al. 2011) and 1 GPa (Falloon et al. 2008) in Table 6. The near-solidus melt compositions range from basaltic at 1 GPa to komatiitic at 7 GPa. In these solidus melts, both MgO and FeO contents increase with increasing pressure, and the Al_2O_3/TiO_2 ratio decreases with increasing pressure. The CaO contents in these near-solidus melts remain relatively constant. The alkali contents in these melts decrease with pressure. Given that the compositions of the near-solidus melts obtained in high-pressure melting experiments range from basaltic to komatiitic, we compared these compositions to those of natural basalts and komatiites (Fig. 5). The near-solidus melt at 3 GPa is picritic and has an intermediate Al_2O_3/TiO_2 ratio and FeO content, which falls between those for the near-solidus melts at 1 and 7 GPa.

Table 4 Summary of experiment results

	Run number	Iteration step	Added melt (wt%)	*T* (°C)	Duration (h)	Equilibrium assemblage	Phase proportions*				R^{2a}	K_D [b]	Fe-loss (%)
KLB-1							ol	cpx	gt	liq			
	5K2353	–	–	1700	4.5	ol, cpx, gt	63.3	22.8	13.9	–	0.40	–	0.0
	1K1976	–	–	1750	3.0	ol, cpx, gt, liq	62.6	24.5	13.0	trace	1.49	–	0.7
	1K1975	–	–	1800	0.3	ol, melt	35.4	–	–	64.6	2.39	$0.35_{(+0.03,\ -0.07)}$	1.4
MISE													
	1K2019	1	14	1750	1.5	ol, cpx, gt, liq	54.0	9.8	8.2	28.1	0.01	$0.34_{(+0.05,\ -0.05)}$	–
	1K2042	2	20	1750	1.5	ol, cpx, gt, liq	47.0	18.2	8.6	26.1	0.01	$0.35_{(+0.1,\ -0.07)}$	–
	1K2055	3	20	1750	1.5	ol, cpx, gt, liq	41.4	11.2	4.6	42.7	0.04	$0.36_{(+0.08,\ -0.07)}$	–
	1K2116	4	20	1750	1.5	ol, cpx, gt, liq	46.2	13.6	8.0	32.2	0.11	$0.37_{(+0.07,\ -0.06)}$	–
	1K2141	5	20	1750	1.5	ol, cpx, gt, liq	51.4	19.0	12.5	17.1	0.38	$0.33_{(+0.09,\ -0.06)}$	–

Abbreviations: ol olivine, *cpx* clinopyroxene, *grt* garnet, *liq* quenched liquid
[a]Sum of squared residuals in mass-balance calculations
[b]Fe–Mg exchange coefficients between residual olivine and quenched melt. The maximum and minimum values were calculated from errors (1σ) on FeO and MgO contents in olivine and quenched liquid

The FeO content of the near-solidus melt at 3 GPa is about 10 wt%, which is not significantly different from ocean island basalts (OIB) from Isua, Greenland. At 7 GPa, the near-solidus melt has an Al_2O_3/TiO_2 ratio of about 2, which is much lower than that of Al-depleted komatiites, and has a higher FeO content than all of the komatiites. The near-solidus melts at 1 and 7 GPa have FeO contents lower than Archean MORB rocks and higher than Archean komatiites. The differences in FeO contents between the near-solidus melts obtained from high-pressure melting experiments and Archean rocks can be explained by their differences in degree of partial melting. Herzberg and O'Hara (2002) constructed forward models to constrain the potential primary melt compositions of mantle peridotites, in particular FeO and MgO contents, by parameterization of experimental data up to 7 GPa. According to their calculations, the FeO content in a melt decreases with decreasing melt fraction below 3 GPa, whereas it increases with decreasing melt fraction above 3 GPa. If it is assumed that the Archean MORB melts were generated at high melt fractions at low pressures below 3 GPa and that the Archean komatiites were generated at high melt fractions in hot plumes at high pressures above 3 GPa, then the differences in FeO contents observed between the experimental near-solidus melt and the Archean rocks are consistent with the results of Herzberg and O'Hara (2002). Figure 6 shows the K_2O and P_2O_5 contents of the solidus melt at 7 GPa as compared to those of lunar KREEP rocks (Ryder 1976; Irving 1977; Ryder et al. 1977), normal MORB (N-MORB), and enriched MORB (E-MORB) (Klein 2004). The K_2O and P_2O_5 contents of the solidus melt at 7 GPa are almost identical to those of N-MORB at the Mid-Cayman Ridge and different from those of lunar KREEP rocks. Assuming that the EER formed as a near-solidus melt, the EER is expected to have had a composition within the range shown in Table 6. The probable pressure of the EER formation in the Hadean Earth and the potential major element composition of the EER are discussed in a later section.

Estimation of the density of the near-solidus melt

In this section, we estimate the density of the near-solidus melt and primitive peridotite to examine whether the EER would have sunk into the mantle or ascended to the surface. The method for estimating the density of the melt and mantle peridotite is from Matsukage et al. (2005a, b).

The density of a melt can be constrained with the molar mass, molar fraction, and partial molar volume of melt component oxides (Bottinga and Weill 1970):

$$\rho = \sum X_i M_i / \sum X_i \overline{V}_i \quad (4)$$

where ρ is density, X_i is mole fraction, $\overline{V}_i$ is partial molar volume, and M_i is the formula weight of component *i*. The values for $\overline{V}_i$ should be calculated at the target pressure and temperature. Here, we only obtained the $\overline{V}_i$ of SiO_2, Al_2O_3, FeO, MgO, and CaO at the target pressure and temperature, since the other minor elements only have a negligible effect on density. In order to obtain the $\overline{V}_i$ values of the five oxides, we need five or more independent relationships between $\overline{V}_i$ and ρ. Therefore, we used five melts whose compositions range from basaltic to peridotitic and densities have been determined by high-pressure and high-temperature experiments in previous studies (Appendix 3). Given that these densities have been determined at different pressures and temperatures from our target pressure and temperature, we calculated the pressure and temperature dependence

Table 5 Compositions of MISE run products

wt%	melt	s.d.	ol	s.d.	cpx	s.d.	gt	s.d.
Iteration 1								
n	5		25		23		25	
SiO_2	45.4	1.0	41.6	0.2	56.4	0.3	44.2	0.3
TiO_2	1.1	0.3	0.0	0.0	0.1	0.0	0.3	0.1
Al_2O_3	5.2	0.5	0.2	0.0	2.7	0.1	21.3	0.8
Cr_2O_3	0.3	0.1	0.1	0.0	0.3	0.1	1.2	0.3
FeO	11.6	0.5	8.5	0.3	4.7	0.3	5.9	0.4
MnO	0.3	0.0	0.1	0.0	0.1	0.0	0.2	0.1
MgO	22.8	1.4	48.9	0.4	25.4	0.7	22.9	0.5
CaO	8.6	0.6	0.3	0.0	9.2	0.8	4.6	0.4
Na_2O	1.2	0.1	0.1	0.0	0.9	0.1	0.1	0.1
K_2O	1.3	0.2	0.0	0.0	0.0	0.0	0.0	0.1
P_2O_5	1.3	0.1	0.0	0.0	0.0	0.0	0.2	0.1
Total	99.1		99.8		99.9		100.8	
Mg#	77.7		91.0		91.0		87.0	
Iteration 2								
n	10		20		20		20	
SiO_2	44.8	1.5	41.2	0.2	55.6	0.2	43.4	0.2
TiO_2	1.8	0.4	0.0	0.0	0.2	0.0	0.8	0.1
Al_2O_3	5.3	0.5	0.2	0.0	3.1	0.1	21.6	0.4
Cr_2O_3	0.3	0.1	0.1	0.1	0.4	0.1	1.4	0.5
FeO	12.6	1.5	9.4	0.4	4.9	0.2	6.6	0.3
MnO	0.2	0.0	0.1	0.0	0.2	0.0	0.2	0.0
MgO	23.9	1.6	50.3	0.5	24.2	1.1	22.7	0.3
CaO	8.4	1.0	0.3	0.1	11.3	1.0	5.3	0.3
Na_2O	1.1	0.1	0.1	0.0	1.0	0.1	0.1	0.0
K_2O	1.0	0.1	0.0	0.0	0.1	0.0	0.0	0.0
P_2O_5	0.4	0.1	0.0	0.0	0.0	0.0	0.2	0.0
Total	99.9		101.8		101.0		102.2	
Mg#	77.2		91.0		90.0		86.0	
Iteration 3								
n	31		31		30		27	
SiO_2	46.2	0.8	41.3	0.3	56.2	0.6	44.1	0.3
TiO_2	0.7	0.2	0.0	0.0	0.1	0.0	0.3	0.1
Al_2O_3	5.9	0.5	0.2	0.0	2.8	0.1	21.3	0.7
Cr_2O_3	0.3	0.1	0.1	0.1	0.3	0.1	1.4	0.2
FeO	11.8	1.1	8.2	0.2	4.9	0.3	5.7	0.5
MnO	0.2	0.1	0.1	0.0	0.1	0.0	0.2	0.0
MgO	26.2	2.2	50.7	0.3	28.3	1.2	24.0	0.6
CaO	7.5	0.7	0.3	0.0	7.4	0.8	4.3	0.6
Na_2O	0.9	0.1	0.1	0.0	0.7	0.0	0.1	0.0
K_2O	0.3	0.1	0.0	0.0	0.0	0.0	0.0	0.0
P_2O_5	0.2	0.0	0.0	0.0	0.0	0.0	0.0	0.0
Total	100.3		101.0		100.8		101.5	
Mg#	79.8		92.0		91.0		88.0	
Iteration 4								
n	40		23		21		22	
SiO_2	45.5	0.6	40.9	0.2	55.6	0.4	43.7	0.4
TiO_2	0.8	0.2	0.0	0.0	0.1	0.0	0.4	0.2
Al_2O_3	5.6	0.2	0.2	0.0	2.6	0.1	21.4	0.2
Cr_2O_3	0.3	0.1	0.1	0.0	0.3	0.1	1.3	0.2
FeO	12.1	0.6	9.0	0.7	4.8	0.2	5.8	0.4
MnO	0.2	0.1	0.1	0.0	0.1	0.0	0.2	0.1
MgO	24.6	0.8	49.6	0.6	26.0	1.1	23.2	0.5
CaO	8.3	0.4	0.3	0.0	9.6	1.2	4.6	0.4
Na_2O	1.0	0.1	0.1	0.0	0.7	0.1	0.1	0.0
K_2O	0.5	0.1	0.0	0.0	0.0	0.0	0.0	0.0
P_2O_5	0.2	0.0	0.0	0.0	0.0	0.0	0.1	0.0
Total	99.0		100.3		100.0		100.7	
Mg#	76.8		90.7		90.5		85.8	
Iteration 5								
n	5		15		15		15	
SiO_2	45.0	1.6	41.5	0.4	56.7	0.3	44.3	0.5
TiO_2	1.6	0.1	0.0	0.0	0.1	0.0	0.8	0.4
Al_2O_3	4.3	0.5	0.2	0.0	2.4	0.1	20.9	0.5
Cr_2O_3	0.2	0.1	0.1	0.0	0.3	0.1	1.0	0.4
FeO	14.5	1.6	9.7	0.2	5.0	0.4	6.7	0.4
MnO	0.3	0.1	0.1	0.1	0.1	0.0	0.2	0.0
MgO	24.1	1.7	48.4	0.6	24.3	0.9	22.6	0.8
CaO	8.1	1.0	0.3	0.1	10.3	0.9	4.6	0.7
Na_2O	1.1	0.1	0.1	0.0	0.9	0.0	0.1	0.0
K_2O	0.3	0.0	0.0	0.0	0.1	0.0	0.0	0.0
P_2O_5	0.3	0.0	0.0	0.0	0.0	0.0	0.1	0.1
Total	100.0		100.4		100.3		101.3	
Mg#	74.8		90.0		90.0		85.8	

of these densities and applied Eq. (4) to the five compositions at the target pressure and temperature. In estimating the pressure dependence, we used the third-order Birch–Mürnaghan equation of state (Birch 1947). Temperature dependence was calculated with the following method. After pressure compensation, values of densities at the target pressure were obtained at different temperatures for three of the five melt compositions. We calculated the temperature dependence of density in these melts by averaging the results, based on the assumption that differences in melt composition are not significant. We then calculated the density at the target pressure and temperature for these five melts. Finally, we applied Eq. (4) to these five

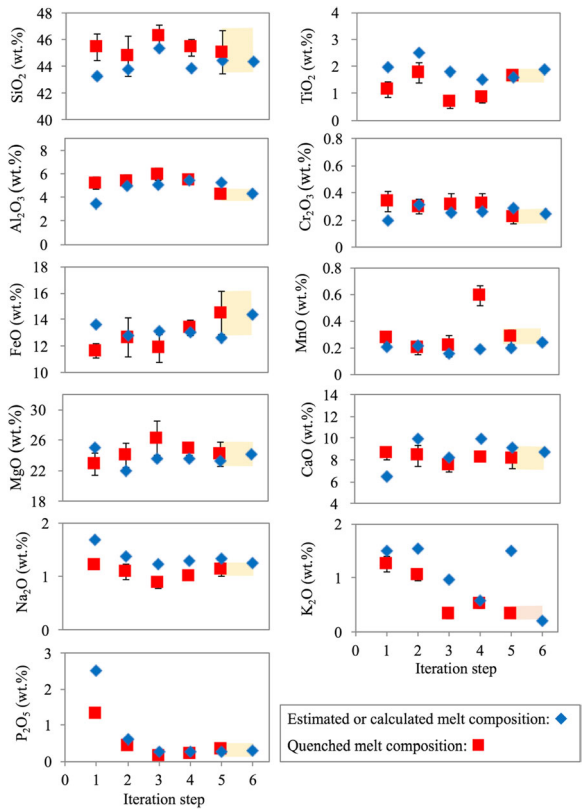

Fig. 3 Compositions of quenched and calculated melts. *Blue diamonds* show the estimated or calculated melt compositions, and *orange squares* show the quenched melt compositions. The *error bars* on the quenched melt compositions are the standard deviation (1σ). *Orange horizontal boxes* show the range of the standard deviations (1σ) of the quenched melt compositions after the 5th iteration. The quenched melt composition after the 5th iteration and the calculated mean composition after the 6th iteration are almost identical (see text for details)

melt compositions and densities at the target pressure and temperature and obtained the $\overline{V}_i$ values of the five oxides. Finally, the density of the near-solidus melt with compositions at the target pressure and temperature was calculated using these $\overline{V}_i$ values.

The density of the primitive peridotite was determined from the density of the minerals that are stable at the target pressure and temperature. We used thermoelastic parameters for forsterite, fayalite, pyrope, almandine, grossular, orthoenstatite, orthoferrosilite, diopside, and hedenbergite (Matsukage et al. 2005b). The solidus mineral assemblage and composition were taken from Davis et al. (2011) at 3 GPa and from our experimental result at 7 GPa. In the lherzolite melting experiments at 1 GPa in Falloon et al. (2008), spinel and plagioclase were present at sub-solidus conditions but were ignored in this calculation because of their minor abundance and negligible effect on density. Pressure can be calculated as the sum of static P_{st} and thermal pressures ΔP_{th}. The static and thermal pressures in our study were calculated with the third-order Birch–Mürnaghan and Mie–Grüneisen equations of state, respectively (Matsukage et al. 2005b).

Figure 7 shows the results of the calculated densities. The densities of the near-solidus melts are lower than the densities of the primitive peridotite. Therefore, an EER formed as a near-solidus melt should have ascended to the surface. The detail of this model is discussed in the next section.

Discussion

A scenario for the formation of the EER in the Hadean

From the difference in $^{142}Nd/^{144}Nd$ ratios between chondrites and the ASE, we conclude that the EER could have formed as a near-solidus melt in the shallow upper mantle within 33.5 Myr of Solar System formation. The extremely small degree of melting in the Hadean mantle would require specific circumstances that allowed the melt to segregate immediately after its generation. One such scenario is shown in Fig. 8 where adiabatically upwelling mantle melts at the pressure and temperature where the mantle geotherm crosses the solidus. If the base of the lithosphere happens to exist just above this depth, then any further mantle upwelling and melting will be prevented, and the near-solidus melt will segregate and ascend into the lithosphere.

Could such a process involving an extremely small degree of partial melting just under a thick lithospheric lid have occurred in the early Hadean? The thickness of the lithosphere largely depends on the style of mantle convection, and so we first examine the style of mantle convection in the early Hadean. Solomatov (1995) showed that thermal convection is exhibited in the stagnant-lid regime when viscosity is dependent on temperature to a sufficiently high degree, and that Earth's mantle and both H_2O-free and H_2O-saturated olivine also have highly temperature-dependent viscosities, which inevitably result in the development of stagnant-lid convection. Thus, Earth's mantle is expected to have been in the stagnant-lid convection regime prior to the onset of the plate tectonics. The timing of the onset of plate tectonics is still debated, but recent studies have proposed that convection of the Hadean mantle in the stagnant-lid regime possibly involved intermittent drip-like subduction (Foley et al. 2014; O'Neil and Debaille 2014). A tectonic regime of stagnant-lid convection with intermittent subduction has been supported by results from multiple analytical studies on Jack Hill zircons (Hopkins et al. 2010; Kemp et al. 2010; Tarduno et al. 2015). Hopkins et al. (2010) estimated the temperature and pressure conditions for the formation of Jack Hill zircons using the Ti-in-zircon thermometer and the phengite, Al-in-hornblende, and Ti-in-quartz barometers. From the estimated pressure and temperature conditions of zircon formation, they obtained

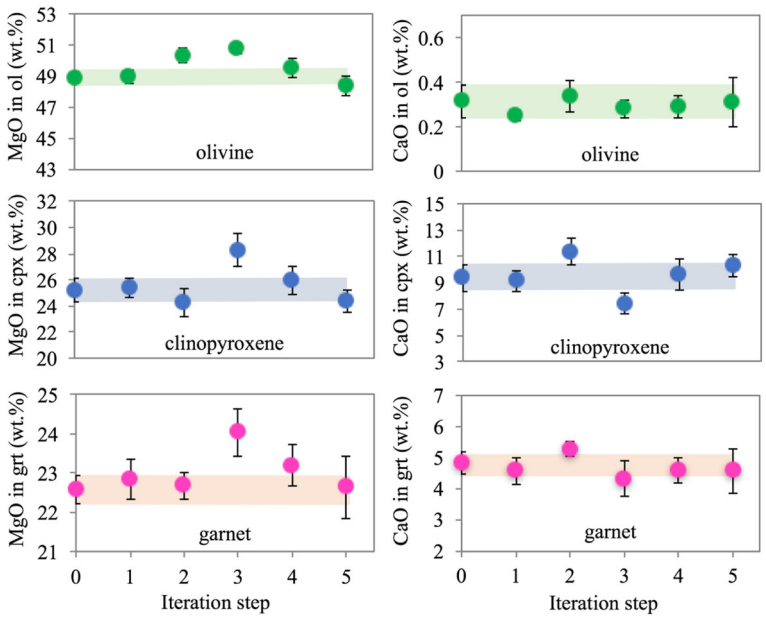

Fig. 4 Convergence of the chemical compositions of residual minerals. The chemical compositions at iteration step 0 represent the chemical compositions of the minerals at the solidus. *Horizontal shaded bars* show the range of the standard deviations (1σ) of the chemical compositions of the minerals at the solidus. After the 5th iteration, the chemical compositions of the residual minerals converge to their respective compositions at the solidus

a near-surface heat flux of <40–85 mW/m^2. This low near-surface heat flux could characterize a convergent margin (Hopkins et al. 2010), rigid plate tectonics (Korenaga 2011), stagnant-lid model (Condie and O'Neill 2010), or heat-pipe model (Moore and Webb 2013). Kemp et al. (2010) investigated the Pb and Hf isotopic compositions of Jack Hill zircons. They calculated the residence time of the protolith of the Jack Hill zircons to be ca. 400 Myr and argued that the protolith was a mafic crust. O'Neill et al. (2013) argued that the long residence time of the protolith of the Jack Hill zircons provides support for the stagnant-lid convection model with intermittent subduction in the Hadean era. Tarduno et al. (2015) showed that the paleomagnetic intensity of 3.3–4.2 Ga Jack Hill zircons was 1.0–0.12 times that of the present-day value. The strength of the magnetic field depends on the heat flux across the core–mantle boundary, which in turn depends on the subduction of a slab. When subduction is sluggish, heat flux across the core–mantle boundary decreases, resulting in a weakened geodynamo. The low paleomagnetic intensity in the Hadean and the early Archean may be a manifestation of intermittent subduction in the stagnant-lid regime. Based on the model of mantle convection and data from Hadean zircons, it is probable that the mantle was in a stagnant-lid convection mode at the time of formation of the EER i.e., within 30 Myr of Solar System formation.

Table 6 Compositions of near-solidus melts at 1, 3, and 7 GPa

wt%	7 GPa[a]	3 GPa[b]	1 GPa[c]
SiO_2	44.3	44.8	51.5
TiO_2	1.9	2.5	1.5
Al_2O_3	4.3	12.7	19.1
Cr_2O_3	0.2	0.1	0.1
FeO	14.4	9.7	5.4
MnO	0.2	0.1	0.1
MgO	24.2	15.8	8.3
CaO	8.8	10.8	9.4
Na_2O	1.3	2.5	4.4
K_2O	0.2	1.0	–
P_2O_5	0.3	–	–
Total	100.1	100.0	99.6
Melt fraction	~0 %	~0 %	2.6 %

[a]This study
[b]Davis et al. (2011)
[c]Falloon et al. (2008)

The next question that follows is whether or not a thick lithosphere could have existed in the stagnant-lid convection regime in the early Hadean. Under stagnant-lid convection with temperature-dependent viscosity, the thickness of the lithosphere decreases as the mantle potential temperature (MPT) increases (Korenaga 2009b). However, Korenaga (2009b) showed that when the effects of the partial melting of the mantle, principally dehydration-stiffening and minimal compositional buoyancy of the lithosphere, are taken into consideration, the lithospheric thickness would increase as the MPT increases, with deepening of the initiation of melting. In the dehydration-stiffening model of Korenaga (2009b),

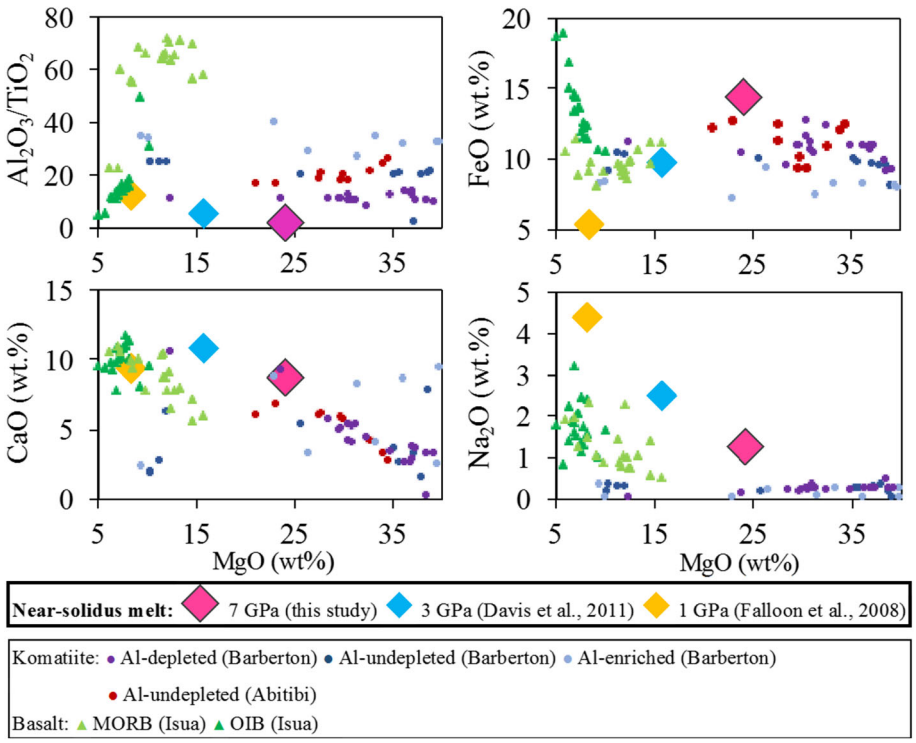

Fig. 5 Comparison of the major element compositions of the 1, 3, and 7 GPa near-solidus melts (Falloon et al. 2008; Davis et al. 2011; this study) with the 3.3–3.5 Ga Barberton komatiites (Robin-Popieul et al. 2012), 2.7 Ga Abitibi komatiites (Kerrich and Xie 2002), and 3.8 Ga Isua MORB and OIB (Komiya et al. 2004). *MORB* mid-ocean ridge basalt, *OIB* ocean island basalt

the base of the lithosphere inevitably coincides with the depth where melting is initiated. Foley et al. (2014) also showed that the viscosity and thickness of the lithosphere increases with increasing MPT due to fast grain growth and healing of lithospheric damage. Although the effects of partial melting of the mantle were not investigated in Foley et al. (2014), this would have enhanced the grain growth in the residual mantle and increased the thickness of the lithosphere up to the depth of the initiation of melting. Thus, a stable, thick lithosphere in the stagnant-lid convection regime can be facilitated by both dehydration-stiffening due to partial melting and by grain growth at high MPT. In both mechanisms, the base of the lithosphere would have been located at the depth where partial melting is initiated. As such, very small degrees of melting would inevitably have occurred in the early Hadean stagnant-lid convection regime.

The dehydration-stiffening proposed by Korenaga (2009b) is based on an assumption that the difference in the viscosities between wet and dry mantles is large, by up to three orders of magnitude (Korenaga 2009). This assumption is based on experimental and theoretical studies on the deformation of olivine aggregates (Fo = 90) (Karato et al. 1986; Hirth and Kohlstedt 1996; Mei and Kohlstedt 2000a, b; Jung et al. 2006; Korenaga and Karato 2008), which showed enhanced dislocation and diffusion creep rates in olivine aggregates with the incorporation of water. In the Korenaga (2009) model, experiments with pure forsterite are excluded because the kinetic properties are expected to be significantly different between forsterite (Fo = 100) and mantle olivine (Fo = 90; McDonough and Sun 1995; Mei and Kohlstedt 2000a). However, Fei et al. (2013) showed that the effect of water on mantle viscosity would be smaller than estimated in previous experiments, based on experimentally obtained Si self-diffusion coefficients in single forsterites. Fei et al. (2013) argued that previous experiments using olivine aggregates had been performed in water-oversaturated conditions, which may have been present at grain boundaries and thereby caused grain boundary sliding, resulting in the overestimation of the effect of water. It is still unclear which of these two arguments is valid with regards to the effect of H_2O on olivine rheology.

Assuming that the dehydration-stiffening model proposed by Korenaga (2009b) is correct, any discrepancy existing between the dehydration-stiffening model and our high-pressure melting experiment would arise from differences in water content. In Korenaga (2009b), the dehydration-stiffening is based on the assumption that

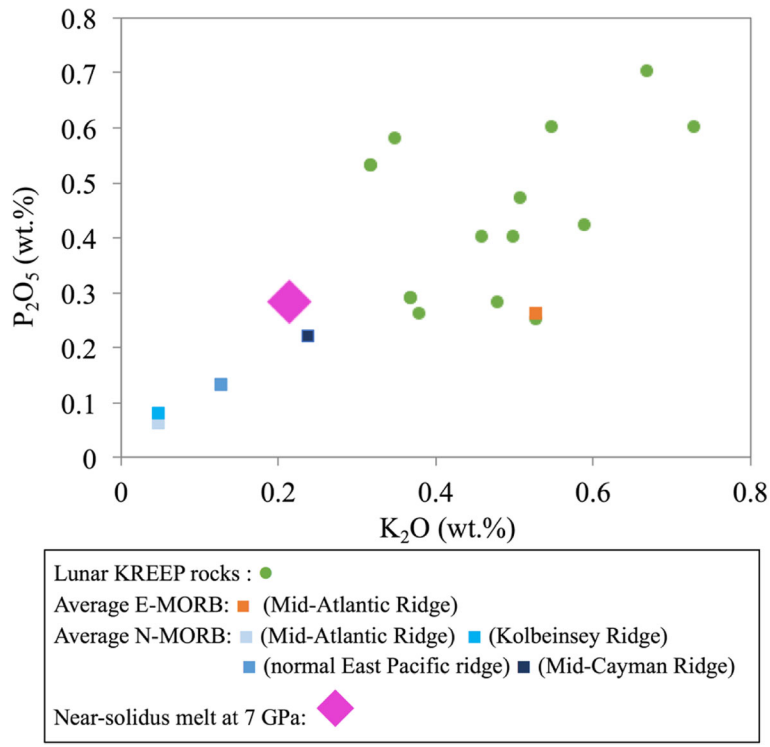

Fig. 6 Comparison of the K_2O and P_2O_5 contents of the 7 GPa near-solidus melt with that of lunar KREEP rocks (Ryder 1976; Ryder et al. 1977; Irving 1977) and average normal (N-) and enriched (E-) MORB (Klein 2004). The N-MORB data are for the Kolbeinsey, normal East Pacific, and Mid-Cayman ridges. The E-MORB data are for the Mid-Atlantic Ridge

asthenospheric olivine contains <1000 ppm H/Si. In our experiments, the synthesized starting materials also contained a trace amount of H_2O (up to 800 ppm). Therefore, no significant discrepancies are expected to exist between the Korenaga model and our high-pressure melting experiment. While such trace amounts of water have negligible influence on the melting phase relations (Green et al. 2014), they can have a strong effect on viscosity (Hirth and Kohlstedt 1996; Mei and Kohlstedt 2000a, b; Korenaga and Karato 2008). Even if the effect of dehydration-stiffening is smaller than that assumed in Korenaga (2009) and fails to produce a sufficiently thick lithosphere, such a thick stagnant-lid could still be generated by fast grain growth and healing of lithospheric damage (Foley et al. 2014). Thus, we conclude that a thick lithosphere may have plausibly existed in the Hadean.

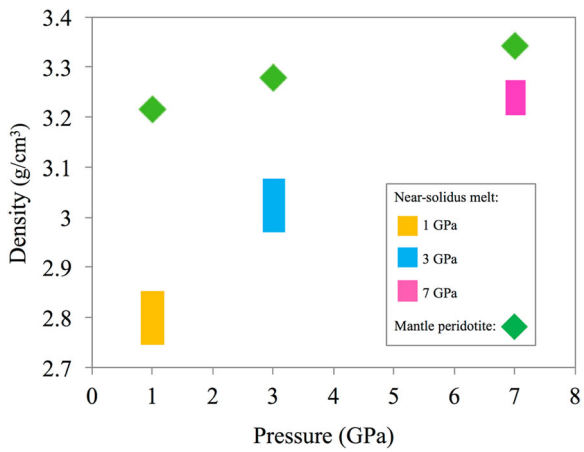

Fig. 7 Densities of the solidus melt and mantle peridotite at 1, 3, and 7 GPa. *Diamonds* and *rectangles* show densities of the primitive peridotite and densities of the near-solidus melts, respectively. The solidus melts are less dense than the mantle peridotite. Therefore, the solidus melts should ascend in the mantle

The composition of the near-solidus melt depends on the thickness of the lithosphere and the depth of the initiation of partial melting, which in turn depends on the MPT (Fig. 6). The MPT from the Phanerozoic to the early Archean has been estimated to range from 1400 to 1600 °C, based on the MgO content of basalts that were interpreted to have been generated by adiabatic melting of the ambient mantle (Komiya et al. 2004; Herzberg et al. 2010). Korenaga (2011) calculated the thermal budget and MPT in plate tectonic convection from the present day to the Hadean and estimated the MPT at 4 Ga to be 1600 °C. The timing of the shift in mantle convection from the stagnant-lid to plate tectonic regime still remains

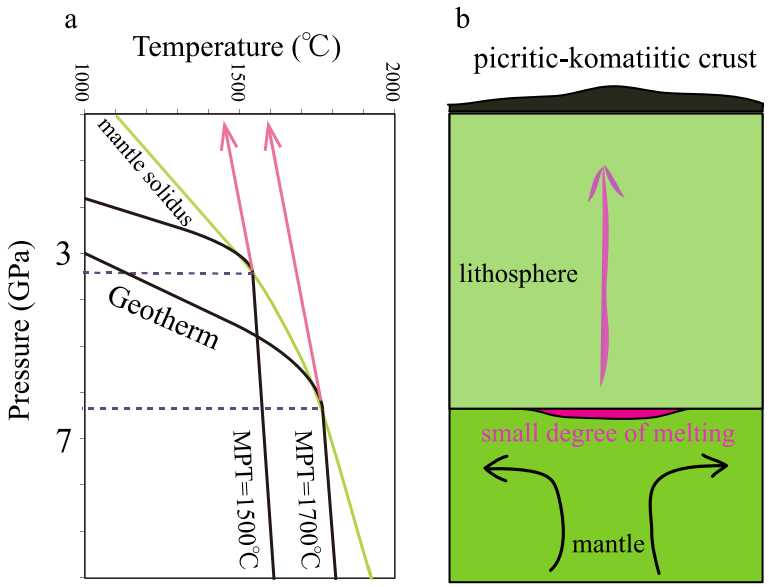

Fig. 8 A proposed scenario for the formation of the EER melt in the Hadean mantle. **a** The Hadean geotherm (temperature gradient from Katsura et al. 2004) and solidus of primitive peridotite (Herzberg et al. 2000). The Hadean mantle potential temperature (MPT) is assumed to have been sufficiently high (1500 to 1700 °C) to initiate partial melting at higher pressure. **b** A schematic diagram of the formation of the EER melt. A small melt fraction needed for EER formation can be generated at the base of thick lithosphere where melting starts. Even at very low degrees of melting, melt can segregate immediately after its generation beneath the base of the thick lithosphere

unclear, but previous studies have suggested that plate tectonics could have started by 4 Ga (Korenaga 2013). Thus, we adopt the MPT at 4 Ga estimated by Korenaga (2011) and assume a range in the MPT from 1500 to 1700 °C for the Hadean mantle. When the MPT is 1500 to 1700 °C, melting in the mantle would initiate between 3 and 7 GPa, and the near-solidus melt would also be generated in this pressure range. In this range, the EER would have a picritic to komatiitic composition (Fig. 5).

In order to apply the stagnant-lid convection model to our model, we need to confirm that the source mantle region for the formation of the EER would have experienced adiabatic melting within 33.5 Myr, which is the maximum formation time of the EER after Solar System formation. We calculated the processing time of adiabatic partial melting of a source mantle region under stagnant-lid convection with a MPT of 1500 and 1700 °C, using an equation of velocity scaling (Solomatov and Moresi 2000; Korenaga 2009b). The asymptotic form of velocity scaling was expressed in Korenaga (2009b) as:

$$v^{*}_{\mathrm{rms}} \approx a_{\mathrm{v}} \left(\frac{\mathrm{Ra}_i}{\theta} \right)^{\beta_{\mathrm{v}}}$$

where v_{rms} is root-mean-square velocity for the entire mantle domain and Ra_i is the internal Rayleigh number. θ is the Frank–Kamenetskii parameter defined by Korenaga (2009b) as:

$$\theta = \frac{E\Delta T}{R(T_{\mathrm{s}} + \Delta T)^2},$$

where E is activation energy, R is the universal gas constant, T_s is the surface temperature, and ΔT is the temperature constant across the mantle. a_{v} and β_{v} were calculated from Korenaga (2009) and Solomatov and Moresi (2000), respectively, by fitting the above equation for velocity scaling to their numerical data. As a result of our calculations, the obtained processing time with a MPT of 1500 and 1700 °C is about ca. 4 and 1 Myr, respectively, when a region corresponding to the upper mantle experiences adiabatic melting. When the whole mantle experiences adiabatic melting, the obtained processing time with a MPT of 1500 and 1700 °C is ca. 15 and 5 Myr, respectively. Since these processing times are sufficiently shorter than the maximum formation time of the EER (i.e., 33.5 Myr after Solar System formation), the stagnant-lid convection model can be applied to the formation of the EER for both upper and whole mantle sources at a MPT of 1500 to 1700 °C.

Fate of the EER

Based on the results in the previous sections, we conclude that the EER would have been a proto-crust, which

formed from a melt generated at an extremely small melt fraction that then rapidly ascended through the mantle to the surface (Fig. 8b). The proto-crust would subsequently have become hidden somewhere in, or lost from, the Earth because all of the ASE has higher $^{142}Nd/^{144}Nd$ ratios than chondrites. The fate of the EER depends on the timing of its formation and the last giant impact. The timing of the EER formation was estimated to be within 33.5 Myr of Solar System formation from $^{147}Sm–^{143}Nd$ and $^{146}Sm–^{142}Nd$ systematics (Boyet and Carlson 2005; Caro 2011; this study). The last giant impact is considered to have generated the Moon, and its timing has been investigated from lunar chronology. The oldest lunar zircon U–Pb age is 150 ± 6 Myr after Solar System formation (Nemchin et al. 2009), and this age has been interpreted to be the age of solidification of the lunar magma ocean. The lunar formation age obtained from the $^{147}Sm–^{143}Nd$ and $^{146}Sm–^{142}Nd$ chronology of the ferroan anorthositic suite falls within the range of 60–125 Myr after Solar System formation (Boyet et al. 2015), and the Rb–Sr, $^{147}Sm–^{143}Nd$ and $^{146}Sm–^{142}Nd$, and Lu–Hf chronology of the lunar Mg-suite (plagioclase-rich rocks in the lunar highland crust) fall within the range of 150–200 Myr after Solar System formation (Carlson et al. 2014). Jacobson et al. (2014) determined the timing of the last giant impact to be 95 ± 32 Myr after the formation of the Solar System, by calculating the relationship between the timing of the last giant impact and mass of materials added to Earth after core formation, which was estimated from concentrations of highly siderophile elements in the mantle.

Based on these results, we consider that the EER formation occurred before the last giant impact. If the EER, or the picritic to Fe-rich komatiitic proto-crust, had been subducted back into the Earth's interior, the ensuing giant impact would have rehomogenized the whole mantle (Canup 2004) and the EER should have become re-mixed into the magma ocean, thus erasing the $^{142}Nd/^{144}Nd$ difference between the EER and EDR. Hence, the EER must have been removed from the Earth in order to explain the $^{142}Nd/^{144}Nd$ difference between the ASE and chondrites. This could have been achieved by the last and preceding giant impacts of the Earth and impact-erosion of the proto-crust into space, leaving the remaining mantle (ASE) more depleted than the original Earth composition. The removed terrestrial material may have possibly formed the Moon (Canup 2012; Cuk and Stewart 2012) or a part of the asteroid belt (Bottke et al. 2015), although exploration of the asteroid belt is only in its early stages.

However, if the Moon and Earth had accreted from similar materials having higher Sm/Nd ratios than most chondrites and had experienced stripping of the crust during collisions of planetesimals as argued by Caro et al. (2008) and Caro (2011), the need for an EER and a missing reservoir would be negated altogether. In contrast, in our model, the EER is proposed to have formed before the last giant impact, and a need remains to search for the missing reservoir that is the complement to the EER. If the EER has been hidden in the lunar interior, then it follows that the $^{142}Nd/^{144}Nd$ ratio of the bulk Moon should be lower than that of the ASE. Given that the $^{142}Nd/^{144}Nd$ ratio of the bulk Moon has yet to be precisely determined, there is a need for more $^{142}Nd/^{144}Nd$ data on rocks from the interior of the Moon in order to assess the feasibility of our model and alternatives proposed by Caro et al. (2008) and Caro (2011).

We consider that the scenario outlined in this paper is the most plausible at present. However, the timing of the EER formation was estimated based on the average value of $^{142}Nd/^{144}Nd$ in chondrites. Due to the significant degree of heterogeneity in $^{142}Nd/^{144}Nd$ values of chondrites (Boyet and Gannoun 2013), it is quite possible that the timing of formation of the EER may have been earlier or later than our estimate. We calculated the timing of formation of the EER taking into account the variation of $^{142}Nd/^{144}Nd$ values of chondrites (– 0.20 ± 0.14; Boyet and Carlson 2005). The variation in chondritic $^{142}Nd/^{144}Nd$ ratios has little effect on the maximum melt fraction, but the timing of formation of the EER is delayed as chondritic $^{142}Nd/^{144}Nd$ increases, possibly up to 150 Myr after Solar System formation. Therefore, the formation of the EER could have occurred after the formation of the Moon. If the EER formed after the giant impact, the picritic–komatiitic crust (EER) could have been subducted into the deep mantle and isolated from the convecting mantle until the present. The possible storage area for the subducted EER is the core–mantle boundary layer, but it is still unclear whether the EER could be subducted to the core–mantle boundary and have been stored there without remixing. More precise analyses of $^{142}Nd/^{144}Nd$ ratios of chondrites and the ASE, and a more conclusive determination of the age of the last giant impact are needed for improving our understanding of early Earth differentiation processes.

Conclusions

We estimated the major element composition of the EER by combining $^{142}Nd/^{144}Nd$ isotopic constraints and results of high-pressure melting experiments on primitive peridotite, which we used to construct a possible scenario for the origin and fate of the EER. The formation of the EER is estimated to have occurred within 33.5 Myr of Solar System formation, through partial melting of the mantle at 3–7 GPa at near-solidus temperatures. The melt fraction was most likely quite low (<2.6 %). The near-solidus melt composition at 3 GPa determined experimentally by Davis

et al. (2011) is picritic. The major element composition of the near-solidus melt at 7 GPa determined with the MISE method in this study is more Fe-rich than komatiites and alkali-poor than KREEP rocks. The calculated density of the EER is lower than the density of primitive peridotite. This result supports a scenario in which the EER ascends in the early mantle and forms picritic to komatiitic crust on the Hadean Earth. Since the EER crust is expected to have been generated before the last giant impact, it would have been bombarded by the last giant impact that formed the Moon. Thus, the EER was stripped from Earth and lost into the space, leaving the Earth more depleted than its original composition. However, the EER reservoir has not yet been found, even in the Moon.

Appendix 1: Calculation of the melting phase relations

We used melting phase relations of primitive peridotite at 3 and 7 GPa determined by Walter (1998) and calculated melting phase relations at 1 GPa using previous experimental data (Baker and Stolper 1994). The melting phase relations were calculated from the changes in fractions of coexisting phases with progressive melting (Walter et al. 1995). The calculated melting relations at 1, 3, and 7 GPa are shown below.

At 1 GPa, 0–27 % in the melt fraction:

34 % Opx + 54 % Cpx + 12 % spinel = 78 % melt + 22 % olivine (Baker and Stolper 1994)

At 3 GPa, 0–10 % in the melt fraction:

7 % olivine + 68 % Cpx + 25 % garnet = 84 % melt + 16 % Opx (Walter 1998)

At 7 GPa, 0–38 % in the melt fraction:

26 % olivine + 50 % Cpx + 24 % garnet = 100 % melt (Walter 1998)

Appendix 2: Two-pyroxene thermometry

We assessed the temperature gradient in the capsule using two-pyroxene thermometry (Gasparik 1990). Powders of pure diopside and enstatite were mixed in a ratio of 1:1 and sealed in a Pt capsule. Experiments were performed at 7 GPa and 1500 °C for 26 h. We calculated and constructed the clinopyroxene (cpx)–orthopyroxene (opx) solvus at 7 GPa (Additional file 1: Figure SA1) using the thermodynamic parameters from Gasparik (1990). The compositions of the cpx and opx were homogeneous throughout the entire capsule and, therefore, there is no significant thermal gradient detectable with the two-pyroxene thermometer. The temperature estimated from the thermometer is ca. 1470 °C, which is 30 °C less than that measured with the thermocouple. This is within uncertainty of the experimental data in Gasparik (1989), which was 30 °C. Therefore, we regard the temperature measured with the thermocouple to be the temperature inside the capsule.

Appendix 3: Density data for five melt compositions used in the melt density calculations

In the melt density calculations, five melt compositions shown in Additional file 2: Table SA1 were used. These reference melt compositions range from basaltic to ultramafic, and the respective near-solidus melt compositions at 1, 3, and 7 GPa range from basaltic to picritic. Therefore, it is considered a reasonable approach to calculate the density of these near-solidus melts using the density data of these reference melt compositions by interpolation.

Additional files

Additional file 1: Figure SA1. Compositions of two pyroxenes as a function of temperature at 7 GPa. The composition–temperature relationship was calculated using the thermodynamic parameters from Gasparik (1990). The compositions of pyroxenes are expressed as follows: Cpx X_{di}: $T = -7979.4(X_{di})^3 + 13{,}910(X_{di})^2 - 8706.1(X_{di}) + 3487.3$. Opx X_{di}: $T = -61{,}488(X_{di})^2 + 16{,}552(X_{di}) + 899.07$. (DOCX 5110kb)

Additional file 2: Table SA1. Density data for five melt compositions. (XLSX 37.9kb)

Abbreviations

ASE: Accessible Silicate Earth (part of the silicate Earth from which we can obtain materials for analysis); EER: Early Enriched Reservoir (low-Sm/Nd reservoir which can compensate for the $^{142}Nd/^{144}Nd$ difference between ASE and chondrites); EDR: Early Depleted Reservoir (residual solid produced by the EER formation); CHUR: Chondritic Uniform Reservoir (putative primitive mantle having a chondritic composition); MISE: Modified Iterative Sandwich Experiment (method for determining the composition of a near-solidus melt proposed by Hirschmann and Dasgupta (2007))

Acknowledgements

We express our gratitude to D. Yamazaki, A. Yoneda, and E. Ito at the Institute for Study of the Earth's Interior, Okayama University, for discussions and support during the experimental work. We thank K. Mibe for support in the use of the Karl Fischer Moisture Titrator MKC-610. We are also grateful to S. Ohi for discussions and support during the experimental work. K. Yoshida and T. Hirajima are thanked for discussions and assistance with EPMA analyses. We would also like to thank T. Iizuka, T. Yamaguti, N. Ishikawa, K. Kaneko, M. Dokyu, and A. Ozawa. We are appreciative of two anonymous reviewers for their comments and to Bjorn Mysen for editorial handling. This study was supported by ISEI for Long-Term, Joint-Use Research (to NK and TK) and JSPS KAKENHI 26400514 (to TK).

Authors' contributions

NK conceived and carried out this study and drafted the manuscript. TY helped to design the high-pressure melting experiments. KM took part in the density calculations. TK participated in the design and coordination of this study and helped to draft the manuscript. All authors have read and approved the final manuscript.

Competing interests

The authors declare that they have no competing interests.

Author details

[1]Graduate School of Human and Environmental Studies, Kyoto University, Yoshida-nihonmatsu-tyo, Sakyo-ku, Kyoto 606-8501, Japan. [2]Institute for Planetary Materials, Okayama University, 827 Yamada, Misasa, Tottori 682-0193, Japan.

Received: 23 November 2015 Accepted: 20 July 2016
Published online: 22 August 2016

References

Baker MB, Stolper EM (1994) Determining the composition of high-pressure mantle melts using diamond aggregates. Geochim Cosmochim Acta 58:2811–2827

Birch F (1947) Finite elastic strain of cubic crystals. Phys Rev 71:809–824

Bottinga Y, Weill DF (1970) Densities of liquid silicate systems calculated from partial molar volumes of oxide components. Am J Sci 269:169–182

Bottke WF, Vokrouhlický D, Marchi S, Swindle T, Scott ERD, Weirich JR, Levison H (2015) Dating the Moon-forming impact event with asteroidal meteorites. Science 348:321–323

Boyet M, Carlson RW (2005) ^{142}Nd evidence for early (>4.53 Ga) global differentiation of the silicate Earth. Science 309:576–581

Boyet M, Gannoun A (2013) Nucleosynthetic Nd isotope anomalies in primitive enstatite chondrites. Geochim Cosmochim Acta 121:652–666

Boyet M, Carlson RW, Borg LE, Horan M (2015) Sm–Nd systematics of lunar ferroan anorthositic suite rocks: constraints on lunar crust formation. Geochim Cosmochim Acta 148:203–218

Canup RM (2004) Dynamics of lunar formation. Annu Rev Astron Astrophys 42:441–475

Canup RM (2012) Forming a Moon with an Earth-like composition via a giant impact. Science 338:1052–1055

Carlson RW, Borg LE, Gaffney AM, Boyet M (2014) Rb-Sr, Sm-Nd and Lu-Hf isotope systematics of the lunar Mg-suite: the age of the lunar crust and its relation to the time of Moon formation. Philos Trans R Soc Lond A 372. doi: 10.1098/rsta.2013.0246

Caro G (2011) Early silicate Earth differentiation. Ann Rev Earth Planet Sci 39:31–58

Caro G, Bourdon B, Halliday AN, Quitté G (2008) Super-chondritic Sm/Nd ratios in Mars, the Earth and the Moon. Nature 452:336–339

Condie KC, O'Neill C (2010) The Archean-Proterozoic boundary: 500 My of tectonic transition in Earth history. Am J Sci 310:775–790

Corgne A, Liebske C, Wood BJ, Rubie DC, Frost DJ (2005) Silicate perovskite-melt partitioning of trace elements and geochemical signature of a deep perovskitic reservoir. Geochim Cosmochim Acta 69:485–496

Ćuk M, Stewart ST (2012) Making the Moon from a fast-spinning Earth: a giant impact followed by resonant despinning. Science 338:1047–1052

Dasgupta R, Hirschmann MM (2007) A modified iterative sandwich method for determination of near-solidus partial melt compositions. II. Application to determination of near-solidus melt compositions of carbonated peridotite. Contrib Mineral Petrol 154:647–661

Davis FA, Hirschmann MM, Humayun M (2011) The composition of the incipient partial melt of garnet peridotite at 3 GPa and the origin of OIB. Earth Planet Sci Lett 308:380–390

Drake MJ, Righter K (2002) Determining the composition of the Earth. Nature 416:39–44

Falloon TJ, Green DH, Danyushevsky LV, McNeill AW (2008) The composition of near-solidus partial melts of fertile peridotite at 1 and 1·5 GPa: implications for the petrogenesis of MORB. J Pet 49:591–613

Fei H, Wiedenbeck M, Yamazaki D, Katsura T (2013) Small effect of water on upper-mantle rheology based on silicon self-diffusion coefficients. Nature 498:213–215

Fitoussi C, Bourdon B (2012) Silicon isotope evidence against an enstatite chondrite Earth. Science 335:1477–1480

Foley BJ, Bercovici D, Elkins-Tanton LT (2014) Initiation of plate tectonics from post-magma ocean thermochemical convection. J Geophys Res: Solid Earth 119:8538–8561

Frei D, Liebscher A, Franz G, Wunder B, Klemme S, Blundy J (2009) Trace element partitioning between orthopyroxene and anhydrous silicate melt on the lherzolite solidus from 1.1 to 3.2 GPa and 1,230 to 1,535 °C in the model system Na_2O–CaO–MgO–Al_2O_3–SiO2. Contrib Mineral Petrol 157:473–490

Gasparik T (1989) Transformation of enstatite–diopside–jadeite pyroxenes to garnet. Contrib Mineral Petrol 102:389–405

Gasparik T (1990) A thermodynamic model for the enstatite-diopside join. Am Min 75:1080–1091

Green DH, Hibberson WO, Rosenthal A, Kovács I, Yaxley GM, Faloon TJ, Brink F (2014) Experimental study of the influence of water on melting and phase assemblages in the upper mantle. J Petrol 55:2067–2096

Herzberg C, O'Hara MJ (2002) Plume-associated ultramafic magmas of Phanerozoic age. J Petrol 43:1857–1883

Herzberg C, Raterron P, Zhang J (2000). New experimental observations on the anhydrous solidus for peridotite KLB-1. Geochem Geophys Geosyst 1. doi:10.1029/2000GC000089.

Herzberg C, Condie K, Korenaga J (2010) Thermal history of the Earth and its petrological expression. Earth Planet Sci Lett 292:79–88

Hirschmann MM, Dasgupta R (2007) A modified iterative sandwich method for determination of near-solidus partial melt compositions. I. Theoretical considerations. Contrib Mineral Petrol 154:635–645

Hirth G, Kohlstedt DL (1996) Water in the oceanic upper mantle: implications for rheology, melt extraction and the evolution of the lithosphere. Earth Planet Sci Lett 144:93–108

Hopkins MD, Harrison TM, Manning CE (2010) Constraints on Hadean geodynamics from mineral inclusions in >4Ga zircons. Earth Planet Sci Lett 298:367–376

Irving AJ (1977) Chemical variation and fractionation of KREEP basalt magmas. In Lunar Planet Sci Conf Proc 8:2433–2448

Jackson MG, Carlson RW (2012) Homogeneous superchondritic ^{142}Nd/^{144}Nd in the mid-ocean ridge basalt and ocean island basalt mantle. Geochem Geophys Geosyst 13. doi:10.1029/2012GC004114

Jacobson SA, Morbidelli A, Raymond SN, O'Brien DP, Walsh KJ, Rubie DC (2014) Highly siderophile elements in Earth/'s mantle as a clock for the Moon-forming impact. Nature 508:84–87

Jung H, Katayama I, Jiang Z, Hiraga T, Karato SI (2006) Effect of water and stress on the lattice-preferred orientation of olivine. Tectonophysics 421:1–22

Kanzaki M (1990) Melting of silica up to 7 GPa. J Am Ceram Soc 73:3706–3707

Karato SI, Paterson MS, FitzGerald JD (1986) Rheology of synthetic olivine aggregates: influence of grain size and water. J Geophys Res: Solid Earth 91:8151–8176

Katsura T, Yokoshi S, Song M, Kawabe K, Tsujimura T, Kubo A, Ito E, Tange Y, Tomioka N, Saito K, Nozawa A, Funakoshi KI (2004) Thermal expansion of Mg_2SiO_4 ringwoodite at high pressures. J Geophys Res 109. doi:10.1029/2004JB003094

Kawakami T, Hokada T (2010) Linking PT path with development of discontinuous phosphorus zoning in garnet during high-temperature metamorphism-an example from Luetzow-Holm Complex, East Antarctica. J Min Pet Sci 105:175–186

Kemp AIS, Wilde SA, Hawkesworth CJ, Coath CD, Nemchin A, Pidgeon RT, Verpoort JD, DuFrane SA (2010) Hadean crustal evolution revisited: new constraints from Pb–Hf isotope systematics of the Jack Hills zircons. Earth Planet Sci Lett 296:45–56

Kerrich R, Xie Q (2002) Compositional recycling structure of an Archean super-plume: Nb–Th–U–LREE systematics of Archean komatiites and basalts revisited. Contrib Min Petrol 142:476–484

Kinoshita N, Paul M, Kashiv Y, Collon P, Deibel CM, DiGiovine B, Greene JP, Henserson DJ, Jiang CL, Marley ST, Nakanishi T, Pardo RC, Rehm KE, Robertson D, Scott R, Schmitt C, Tang XD, Vondrasek R, Yokoyama A (2012) A shorter ^{146}Sm half-life measured and implications for ^{146}Sm-^{142}Nd chronology in the solar system. Science 335:1614–1617

Klein EM (2004) Geochemistry of the igneous oceanic crust. In: Holland HD, Turekian KK (ed)Treatise on Geochemistry, Elsevier. Amsterdam 3:433–463

Komiya T, Maruyama S, Hirata T, Yurimoto H, Nohda S (2004) Geochemistry of the oldest MORB and OIB in the Isua Supracrustal Belt, southern West Greenland: implications for the composition and temperature of early Archean upper mantle. Island Arc 13:47–72

Korenaga J (2009a) A method to estimate the composition of the bulk silicate Earth in the presence of a hidden geochemical reservoir. Geochim Cosmochim Acta 73:6952–6964

Korenaga J (2009b) Scaling of stagnant-lid convection with Arrhenius rheology and the effects of mantle melting. Geophys J Int 179:154–170

Korenaga J (2011) Thermal evolution with a hydrating mantle and the initiation of plate tectonics in the early Earth. J Geophys Res 116. doi: 10.1029/2011JB008410

Korenaga J (2013) Initiation and evolution of plate tectonics on Earth: theories and observations. Ann Rev Earth Planet Sci 41:117–151

Korenaga J, Karato SI (2008) A new analysis of experimental data on olivine rheology. J Geophys Res: Solid Earth 113. doi: 10.1029/2007JB005100

Labrosse S, Hernlund JW, Coltice N (2007) A crystallizing dense magma ocean at the base of the Earth's mantle. Nature 450:866–869

Lee CTA, Yin QZ, Lenardic A, Agranier A, O'Neill CJ, Thiagarajan N (2007) Trace-element composition of Fe-rich residual liquids formed by fractional crystallization: implications for the Hadean magma ocean. Geochim Cosmochim Acta 71:3601–3615

Matsukage KN, Jing Z, Karato SI (2005a) Density of hydrous silicate melt at the conditions of Earth's deep upper mantle. Nature 438:488–491

Matsukage KN, Nishihara Y, Karato SI (2005b) Seismological signature of chemical differentiation of Earth's upper mantle. J Geophys Res 110. doi:10.1029/2004JB003504

McDonough WF, Sun SS (1995) The composition of the Earth. Chem geol 120: 223–253
Mei S, Kohlstedt DL (2000a) Influence of water on plastic deformation of olivine aggregates: 1. Diffusion creep regime. J Geophys Res: Solid Earth 105:21457–21469
Mei S, Kohlstedt DL (2000b) Influence of water on plastic deformation of olivine aggregates: 2. Dislocation creep regime. J Geophys Res: Solid Earth 105: 21471–21481
Mibe K, Fujii T, Yasuda A, Ono S (2006) Mg–Fe partitioning between olivine and ultramafic melts at high pressures. Geochim Cosmochim Acta 70:757–766
Moore WB, Webb AAG (2013) Heat-pipe earth. Nature 501:501–505
Nemchin A, Timms N, Pidgeon R, Geisler T, Reddy S, Meyer C (2009) Timing of crystallization of the lunar magma ocean constrained by the oldest zircon. Nature geosci 2:133–136
Nielsen RL, Gallahan WE, Newberger F (1992) Experimentally determined mineral-melt partition coefficients for Sc, Y and REE for olivine, orthopyroxene, pigeonite, magnetite and ilmenite. Contrib Mineral Petrol 110:488–499
O'Neill C, Debaille V (2014) The evolution of Hadean–Eoarchaean geodynamics. Earth Planet Sci Lett 406:49–58
O'Neill C, Debaille V, Griffin W (2013) Deep earth recycling in the Hadean and constraints on surface tectonics. Am J Sci 313:912–932
Qin L, Carlson RW (2016) Nucleosynthetic isotope anomalies and their cosmochemical significance. Geochem J 50:43–65
Ringwood AE (1966) Chemical evolution of the terrestrial planets. Geochim Cosmochim Acta 30:41–104
Robin-Popieul CC, Arndt NT, Chauvel C, Byerly GR, Sobolev AV, Wilson A (2012) A new model for Barberton komatiites: deep critical melting with high melt retention. J Pet 53:2191–2229
Ryder G (1976) Lunar sample 15405: remnant of a KREEP basalt-granite differentiated pluton. Earth Planet Sci Lett 29:255–268
Ryder G, Stoeser DB, Wood JA (1977) Apollo 17 KREEPy basalt: a rock type intermediate between mare and KREEP basalts. Earth Planet Sci Lett 35:1–13
Salters VJ, Longhi J (1999) Trace element partitioning during the initial stages of melting beneath mid-ocean ridges. Earth Planet Sci Lett 166:15–30
Shaw DM (1970) Trace element fractionation during anatexis. Geochim Cosmochim Acta 34:237–243
Solomatov VS (1995) Scaling of temperature-and stress-dependent viscosity convection. Phys Fluid 7:266–274
Solomatov VS, Moresi LN (2000) Scaling of time-dependent stagnant lid convection: application to small-scale convection on Earth and other terrestrial planets. J Geophys Res: Solid Earth 105:21795–21817
Sprung P, Kleine T, Scherer EE (2013) Isotopic evidence for chondritic Lu/Hf and Sm/Nd of the Moon. Earth Planet Sci Lett 380:77–87
Suzuki T, Hirata T, Yokoyama TD, Imai T, Takahashi E (2012) Pressure effect on element partitioning between minerals and silicate melt: melting experiments on basalt up to 20 GPa. Phys Earth Planet Inter 208:59–73
Takahashi E (1986) Melting of a dry peridotite KLB-1 up to 14 GPa: implications on the origin of peridotitic upper mantle. J Geophys Res 91:9367–9382
Takahashi E, Kushiro I (1983) Melting of a dry peridotite at high pressures and basalt magma genesis. Am Min 68:859–879
Tarduno JA, Cottrell RD, Davis WJ, Nimmo F, Bono RK (2015) A Hadean to Paleoarchean geodynamo recorded by single zircon crystals. Science 349: 521–524
Walter MJ (1998) Melting of garnet peridotite and the origin of komatiite and depleted lithosphere. J Pet 39:29–60
Walter MJ, Sisson TW, Presnall DC (1995) A mass proportion method for calculating melting reactions and application to melting of model upper mantle lherzolite. Earth Planet Sci Lett 13:77–90
Weiss BP, Elkins-Tanton LT (2013) Differentiated planetesimals and the parent bodies of chondrites. Ann Rev Earth Planet Sci 41:529–560
Zhang J, Li B, Utsumi W, Liebermann RC (1996) In situ X-ray observations of the coesite-stishovite transition: reversed phase boundary and kinetics. Phys Chem Min 23:1–10